




Synthesis and characterization of aluminum-doped graphitic carbon

Isabelle P. Gordon, Department of Chemistry & Biochemistry, Montana State University, Bozeman, MT 59715, USA
Grace Suenram, Department of Chemistry & Biochemistry, Montana State University, Bozeman, MT 59715, USA; Department of Mechanical & Civil Engineering, California Institute of Technology, Pasadena, CA 91125, USA
Devin McGlamery, and Nicholas P. Stadie , Department of Chemistry & Biochemistry, Montana State University, Bozeman, MT 59715, USA
Address all correspondence to Nicholas P. Stadie at nstadie@montana.edu

(Received 21 December 2023; accepted 5 February 2024)

Abstract

Heteroatom doping of graphitic carbon is of high interest for tuning its physicochemical properties. Aluminum is commonly reported as a high-interest dopant, but few synthetic strategies have been reported owing to the low equilibrium solubility of Al within graphite. Herein we report several strategies to achieve metastable aluminum-substituted turbostratic graphitic carbon materials with aluminum contents up to ~0.5 at%, via co-pyrolysis of two molecular precursors between 800 and 1100°C. The resulting materials exhibit turbostratic graphitic structure and a previously unreported aluminum environment detectable by X-ray absorption spectroscopy (XAS), a likely signature of trigonal planar or puckered AlC_3 -type sites.

Introduction

Substitutional heteroatom doping and co-doping of carbon-based (and other group IV) solids by elements such as boron, nitrogen, phosphorous, and sulfur has been extensively explored to tune the structural and chemical/electrochemical properties for a variety of applications.^[1] Notable examples of this strategy are boron incorporation into graphite for nuclear shielding applications, modification of the electronic structure of fullerenes and nanotubes by B (p-type) and N (n-type) doping, and nitrogen incorporation into templated carbon to enhance CO_2 uptake for direct air capture applications and methane adsorption. In general, this body of research is wide-ranging in its findings, and recently many long-prevailing trends in the results are coming under higher scrutiny. Phosphorous incorporation is relatively common as a strategy to enhance the electron donating character of sp^2 -hybridized carbon surfaces; on the other hand, few experimental reports exist that describe the successful substitutional incorporation of aluminum into a graphitic lattice. Hence, there is fundamental importance in this endeavor given the complementarity of the electron withdrawing/donating properties of Al and P with respect to carbon.

Aluminum and carbon are typically explored together as metal matrix composite (MMC) materials, or in other composite applications (e.g., aluminium nanoparticles on porous carbon supports).^[2] Graphite and aluminium metal face wettability issues when forming composites; the binary phase, aluminum carbide (Al_4C_3) is readily formed at high temperatures.^[3–5] Few existing studies directly target substitutional doping of graphite with aluminium as the dopant. A representative such study, perhaps the first to explicitly report substitutional incorporation of aluminum into an sp^2 -hybridized carbon system, is focused solely on graphene and not a free-standing, bulk material.^[6]

On the contrary, numerous computational studies investigate aluminum doping in carbon materials (e.g., in carbon nanotubes (CNTs),^[7,8] graphite,^[9,10] and graphene^[11–13]) and many predict applications towards hydrogen storage,^[9,13] gas sensing,^[8,12,14–16] and catalysis^[17,18] that would require free-standing, bulk AlC_x materials. The aluminum-carbon binary phase diagram reported by Gokcen and Oden^[19] (Fig. S1) seems to remain the state of knowledge today as to the equilibrium aluminum solubility in crystalline graphite. The precise solubility limit is unknown but is often reported as negligible (which we assign as <0.01 at%). We hypothesized that further investigation via bottom-up synthesis techniques could lead to a variety of ordered or disordered and stable or metastable bulk graphitic materials with higher aluminum content than 0.01 at%, similar to those prepared for other heteroatoms (e.g., boron^[20,21] and phosphorus^[22]).

In this work, we explore a variety of direct (bottom-up from molecular precursors) synthesis approaches targeting high aluminum-content graphitic carbon materials where aluminum is exclusively substituted within the graphitic lattice. Under optimal conditions and after appropriate post-synthesis processing, samples containing up to ≤ 0.5 at% Al could be synthesized and were subsequently characterized. These materials are generally highly disordered, but evidence is presented that the aluminum is likely bound in trigonal planar environments within the graphitic lattice. Challenges of the present synthesis method are also discussed, lending insights for future studies.

Results and discussion

Synthesis

Several synthetic approaches were explored herein in an effort to achieve phase-pure samples of aluminum-substituted

graphitic carbon (AlC_x). The temperature range of interest in this work, informed by previous work in boron.^[20] and phosphorus-doping,^[22] was 800–1100°C. Hence, while the graphitic ordering of such products was expected to only be modest (especially in the stacking direction), the range of heteroatom content was expected to be as high as possible, the primary target of this work. Closed-reactor synthesis in this temperature range typically requires the use of quartz ampules when refractory metal ampules are not available (such as in this laboratory). Hence, all experiments described herein involve the selection of precursors followed by charging into a quartz ampule under inert argon atmosphere, and subsequent heating to a set temperature between 800 and 1100°C.

At all temperatures explored in this work, an undesired byproduct, the aluminosilicate mineral known as mullite ($3\text{Al}_2\text{O}_3 \cdot 2\text{SiO}_2$), was formed during synthesis. This byproduct is attributable to a reaction between the quartz ampule and the Al-containing precursor (e.g., AlCl_3 or TMA). This byproduct could be easily removed by dissolution in aqueous HF (see Fig. S2). Numerous attempts were made to prevent the formation of mullite altogether, including passivation of the quartz ampule with pre-synthesis carbon deposition, the use of a molybdenum packet to isolate the precursors from the quartz, and simply the exploration of dilute Al-doping to prevent excessive leaching of the quartz ampule; nevertheless, none of these strategies were successful in preventing the formation of mullite (more information is given in the Supporting Information). Therefore, the remainder of this study emphasizes the post-HF treated AlCl_3 -derived or TMA-derived AlC_x materials in investigations of structure and composition.

Structure

The crystalline structure of directly synthesized AlC_x was investigated by powder XRD, as shown in Fig. 1. All of the XRD patterns for the pre- and post-HF washed AlC_x materials show a broad reflection centered at $2\theta = 23\text{--}26^\circ$, corresponding to the (002) reflection in graphite. The broadness of this feature indicates the existence of small crystallites and significant long-range disorder in the stacking structure (i.e., turbostratic ordering). Additional well-defined peaks in the pre-HF treated samples are indicative of mullite.^[23] Under otherwise identical conditions, the mullite reflections increase in intensity with increasing Al:C ratio (decreasing x) and with increasing temperature. Mullite formation is likely attributable to side reactions between the aluminum precursor and the quartz ampule, sequestering a portion of the available aluminum and preventing complete incorporation within the graphitic lattice. The mullite reflections completely disappear following HF treatment, indicating that HF dissolution is a viable route to obtain mullite-free AlC_x .

The in-plane structure of the as-synthesized AlC_x materials was further investigated by Raman spectroscopy (Fig. 2). Spatial scanning across the surfaces of the AlCl_3 -derived AlC_x materials revealed two distinct structural environments: more-ordered and more-disordered graphitic carbon, independent of

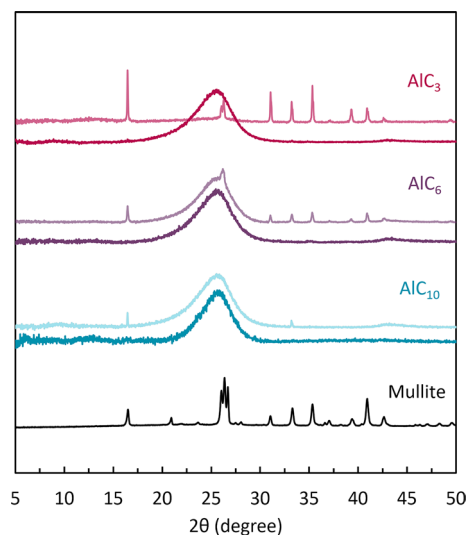


Figure 1. X-ray diffraction patterns of pre- (light trace) and post-HF treated (dark trace) AlCl_3 -derived AlC_x (of nominal composition $x = 3, 6, 10$) compared to a crystalline mullite standard.

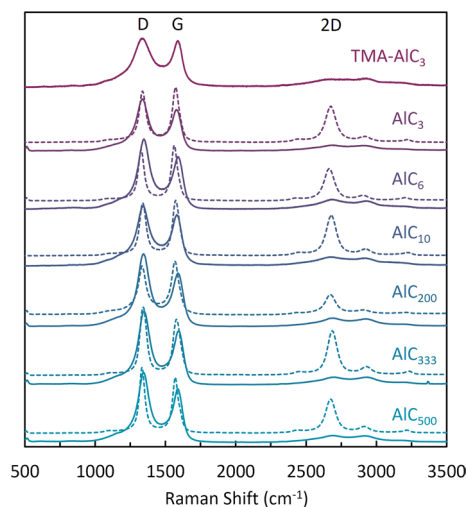


Figure 2. Raman spectra of post-HF treated AlCl_3 - and TMA-derived AlC_x materials under irradiation at 532 nm, showing two distinct types of material in each sample: more-ordered (dashed lines) and more-disordered (solid lines) nanocrystalline graphite.

the nominal composition. Three notable peaks are observed in each spectrum, known as the D peak ($\sim 1340\text{ cm}^{-1}$), G peak ($\sim 1580\text{ cm}^{-1}$), and 2D peak ($\sim 2680\text{ cm}^{-1}$). In regions where the AlC_x is more ordered, the full-width at half-maximum (FWHM) of the D and G peaks are narrow and the 2D region is defined by four well-resolved peaks. In more disordered regions, the D and G peaks are wider, the 2D region is a broad, modulated hump, and the I(D):I(G) ratio is > 1 . These spectral features are quantitatively summarized in Table S2. The more ordered regions may be a result of carbon pyrolysis in the presence of aluminum as a catalyst. The interlayer spacing, as

determined by XRD, is narrower in all AlC_x materials derived by AlCl_3 (e.g., 3.48–3.50 Å at 1100°C) than in pure carbon materials derived under equivalent conditions (e.g., 3.51 Å for neat benzene-derived carbon synthesized at 1100°C) (Fig. S3). Lower aluminum content (e.g., AlC_{10}) correlates with narrower interlayer spacing; hence, the least amount of aluminum in the initial reaction leads to the strongest catalytic effect, likely owing to the formation of mullite in higher Al content reaction mixtures.

Composition and morphology

The elemental composition of directly synthesized (post-HF treated) AlC_x was investigated herein by EDX spectroscopy (Fig. 3). Materials derived from AlCl_3 were determined to have Al contents of 0.1–0.5 at% Al, generally increasing with the nominal composition (i.e., the initial concentration

of Al in the reaction mixture). On the other hand, materials derived from TMA had negligible Al content remaining after HF treatment. These results indicate that there is a significantly larger dependence of the eventual Al content on the identity of the precursor than on the nominal composition of the reaction.

Small traces of chlorine (<1.2 at%) are also found to exist within post-HF washed AlC_x materials; this residual Cl content scales directly with the nominal Cl content provided by the AlCl_3 precursor. EDX mapping confirms that Cl is not preferentially located within the Al-rich regions (Fig. S4) Rather, the Cl is likely trapped between graphitic sheets, as an intercalant, or covalently bonded to the graphitic network, as previously observed.^[22,24] No regions of stoichiometric compositions consistent with mullite are found to exist within post-HF washed AlC_x materials.

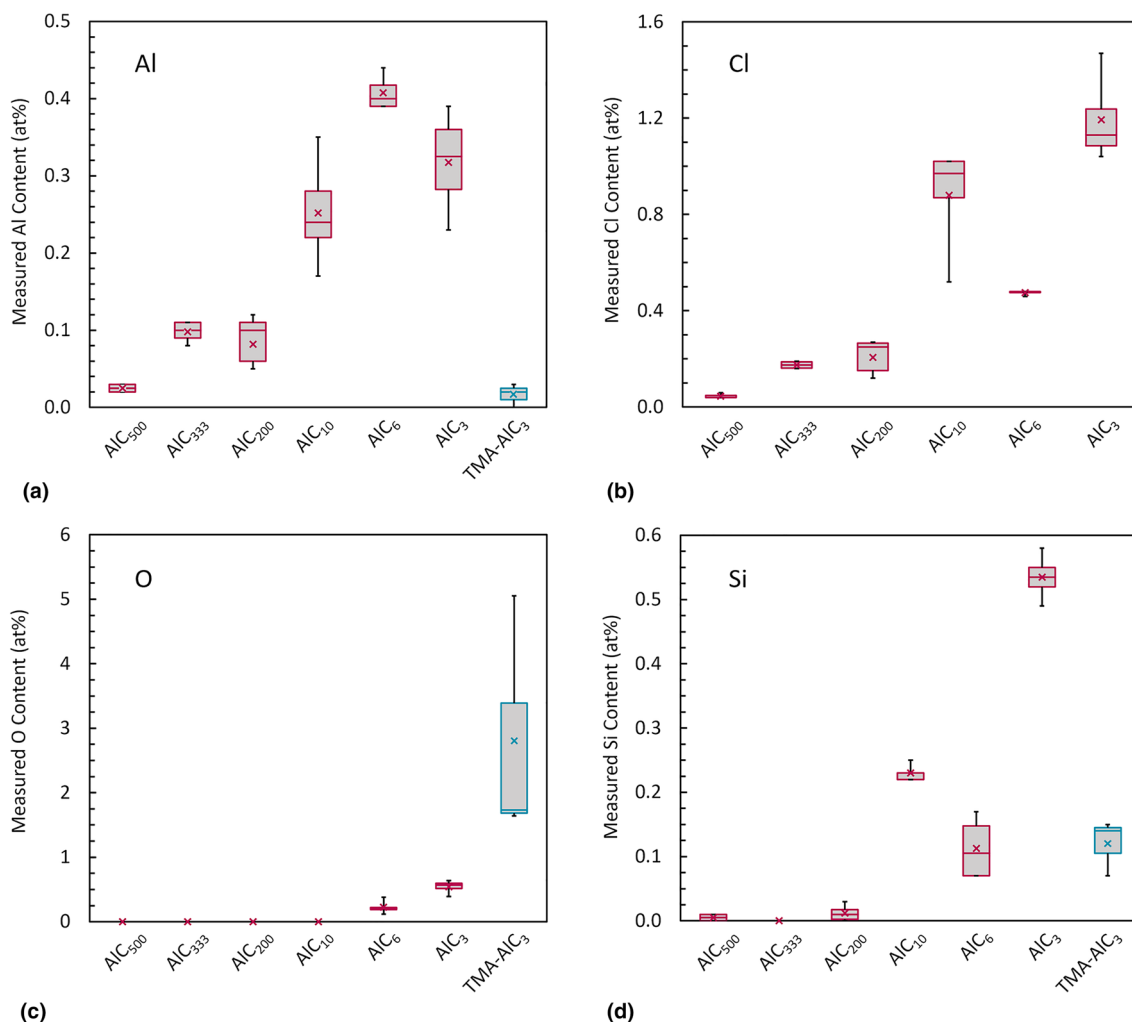


Figure 3. Chemical composition of post-HF treated AlCl_3 - and TMA-derived AlC_x materials as determined by EDX spectroscopy. AlCl_3 - (1100°C) and TMA- (800°C) derived materials are shown in magenta and blue, respectively. The sample names indicate the nominal Al:C ratio in the initial reaction.

X-ray absorption spectroscopy

The chemical environment of aluminum within the highest Al content materials was further investigated by XAS. The XAS spectra at the Al K-edge of both pre- and post-HF treated AlCl_3 -derived AlC_x (of nominal composition $x=3, 6,$ and 10) are shown in Fig. 4. The pre-HF treated samples, included herein for control purposes (since they are known to contain predominantly mullite-type Al), all exhibit an edge and two post-edge features at 1567.4, 1568.7, and 1572.7 eV, respectively, that are consistent with mullite.^[25,26] After HF treatment, a prominent edge feature at 1566.8 eV and a post-edge feature at 1571.7 eV (referred to as E^* and E^\wedge , respectively) arise in all AlC_x materials with >0.2 at% actual Al content (AlC_{10} , AlC_6 , and AlC_3). A slight third feature is evident at 1569.0 eV in AlC_6 . The primary new environments, E^* and E^\wedge , are not consistent with tetrahedral (Td) AlO_4 or octahedral (Oh) AlO_6 environments found in mullite, K10, or AlPO_4 , nor are they consistent with Td AlC_4 environments in Al_4C_3 . The novel environments are rather lower in energy, suggesting a lower aluminum coordination environment,^[27] such as trigonal planar or pyramidal. In general, both E^* and E^\wedge increase in intensity at higher synthesis temperatures [Fig. 4(b)].

The TMA-derived AlC_x plays an important role in this study owing to the inherent presence of Al-C bonds derived from TMA itself, some of which would likely remain intact in the AlC_x product. Indeed, the XAS spectrum of the neat TMA-derived material pyrolyzed at 800°C does in fact exhibit the same E^* and E^\wedge features present in AlCl_3 -derived AlC_x materials [Fig. 4(c)], albeit in lower overall concentration of Al. Interestingly, the TMA-derived samples also contain an Al environment at 1561.3 eV that may be attributed to Al-Al bonding.^[28] This would be consistent with TMA decomposition mechanisms where TMA decomposes to monomethyl aluminum (MMA) and bulk Al metal phase segregation occurs.^[29,30] While we are unable to assign an unambiguous Al bonding environment to E^* and E^\wedge , the existence of these features in AlC_x from both precursors after HF treatment is likely indicative of Al-C bonding in both materials.

Conclusions

Two aluminum-bearing precursors and a wide range of synthetic conditions were explored in an effort to synthesize carbon-rich graphitic materials incorporating Al within the sp^2 -hybridized lattice. All routes followed a single-step, direct

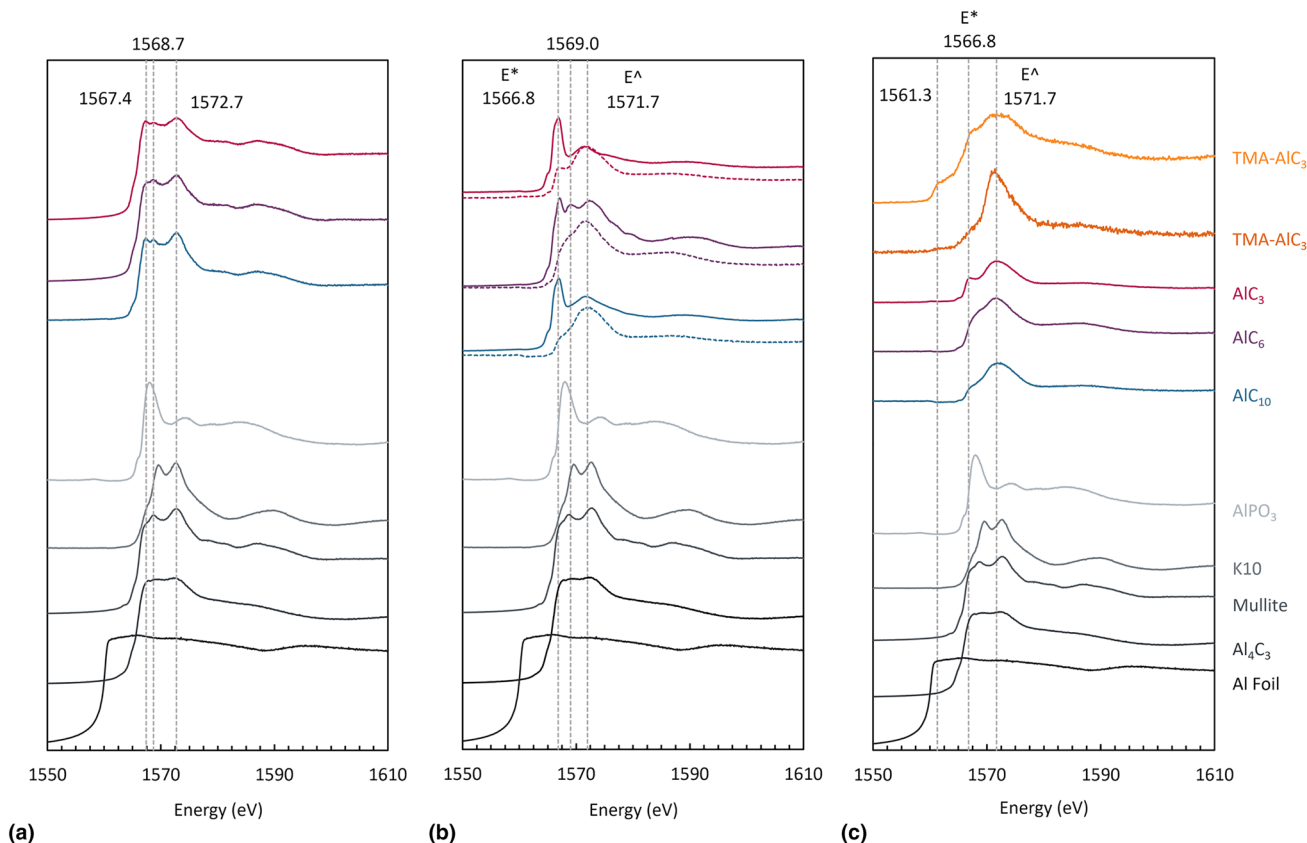


Figure 4. XAS spectra near the Al K-edge of (a) pre- and (b) post-HF treated AlCl_3 -derived AlC_x (where $x=3, 6,$ and 10) AlC_x materials synthesized at 1100°C (solid line) are compared to 800°C (dashed line). (c) XAS Al K-edge spectra of halide- and TMA-derived AlC_x (where $x=3, 6,$ and 10) synthesized at 800°C (dark orange) and 1100°C (light orange). Standards include AlPO_4 , K10, mullite, Al_4C_3 , and Al foil.

synthesis approach that was chosen to favour metastable states with a high Al dopant concentration, at the penalty of low graphitic ordering. The use of a quartz ampule as the closed reaction vessel led to the formation of mullite as an impurity in all reactions studied; this impurity could be effectively removed by post-synthetic dissolution in aqueous HF. The resulting materials were thoroughly characterized, showing that a small content of Al was likely incorporated within the lattice. The presence of Al precursors in the reaction mixture gave rise to a catalytic graphitization resulting in interlayer spacings closer to that in crystalline graphite. Using AlCl_3 as the aluminum precursor, up to ~ 0.5 at% was evidenced across a wide range of initial conditions, indicating that factors such as the temperature and vessel wall chemistry played a larger role than the composition of the initial reaction. Analysis of the XAS spectra obtained for all AlC_x materials with appreciable Al content showed that a pair of new features, at 1567–1572 eV, are a unique signature of such materials and are consistent with the presence of trigonal planar AlC_3 -type environments. Further studies are warranted to examine these features in detail and determine their origin.

Materials and methods

Direct synthesis of AlC_x

Aluminum-doped graphitic materials, hereinafter referred to as AlC_x , were synthesized via a direct synthesis route analogous to previous strategies employed for boron^[20] and phosphorus.^[22] In each case, a quartz ampule (15 cm length, 1.0 cm inner diameter) was charged with either a mixture of benzene (anhydrous 99.8%, Sigma Aldrich) and aluminum trichloride (AlCl_3 , anhydrous, Acros Organics), a solution of trimethylaluminum in toluene (TMA/toluene, 2.0 M, Sigma Aldrich), or neat trimethylaluminum (TMA, 97.0%, Sigma Aldrich), inside a glovebox under inert argon conditions (≤ 0.5 ppm O_2 , ≤ 0.5 ppm H_2O). In certain cases, the ampule was pretreated by carbon passivation (neat benzene pyrolysis inside a double-necked ampule) or the precursors were wrapped in a molybdenum foil ($\geq 99.9\%$, 25 μm thick, Sigma) pouch prior to sealing for the final reaction; such efforts were not found to be more successful than direct pyrolysis within a standard quartz ampule. The total amounts of the precursors were determined by setting the final pressure of the reaction at 20 bar, based on the inner volume of the ampule (~ 12 mL) and the assumptions that pyrolysis would be stoichiometric and all products would be diatomic gases (H_2 , HCl , or Cl_2). A Swagelok ultra-torr adaptor was placed over the open end of the ampule; the capped ampule was removed from the glovebox and partially submerged in liquid nitrogen to solidify the precursor solution. The ampule was connected to a Schlenk line, evacuated to 10^{-3} mbar, and then flame-sealed under vacuum.

Sealed ampules were placed on an elevated platform at the center of a chamber furnace (Carbolite CWF 12/13) and heated to a final set temperature between 800 and 1100°C via a programmable PID controller (Eurotherm 3216). The temperature set point was held for 1 h and then cooled to below 100°C at

which point the furnace was opened and the sealed ampules were removed. Sealed ampules were carefully opened using a diamond-bladed rotary saw in a fume hood where gaseous byproducts (e.g., HCl) could be safely released. The solid product was collected and rinsed with deionized water and acetone. All samples were dried in air at 80°C for 24 h before further analysis. To dissolve aluminosilicate impurities, some samples were subjected to HF washing dissolution in 20% aqueous HF for 48 h, followed by rinsing with copious water. The resulting materials are referred to according to their nominal composition and aluminum precursor, as shown in Table S1.

Materials characterization

Powder X-ray diffraction (XRD) measurements were performed using a Bruker D8 ADVANCE diffractometer using $\text{Cu K}\alpha_{1,2}$ radiation ($\lambda = 1.54$ Å) in reflection geometry. Samples were prepared for XRD by ultrasonication in acetone for 5 min and then drying at 80°C for 24 h. Raman spectroscopy was performed using a Horiba LabRAM HR Evolution spectrometer equipped with a confocal microscope and a frequency-doubled Nd:YAG laser (532 nm) with an incident power of 10 mW. Scanning electron microscopy (SEM) and energy dispersive X-ray (EDX) spectroscopy were measured using a Physical Electronics (PHI) 710 microscope with a field emission source operated at 1 and 10 kV, respectively. Samples were prepared for SEM and EDX by pressing the as-collected material into indium foil which was then secured to an aluminum mount. The actual Al content in each material as measured by EDX is shown in Table S1.

X-ray absorption spectroscopy

Aluminum and carbon chemical environments were analyzed by X-ray absorption spectroscopy (XAS), measured at the Spherical Grating Monochromator (SGM) beamline at the Canadian Light Source (CLS). As-synthesized flakes were mounted on carbon tape and measured under ultra-high vacuum (10^{-9} mbar). Total fluorescence yield (TFY) was measured for each sample by averaging over four silicon drift detectors (SDDs). Several standard materials were mounted for comparison to AlC_x : aluminum foil (0.25 mm thick, 99.999%, Sigma-Aldrich), aluminum carbide (Al_4C_3 , 98%, Goodfellow Corp.), mullite ($3\text{Al}_2\text{O}_3 \cdot 2\text{SiO}_2$, 98%, Alfa Aesar), montmorillonite (K10, Clay Minerals Society), and aluminum phosphate (AlPO_4 , 99.99%, Sigma-Aldrich).

Acknowledgments

We are very grateful to Jonathan Snider for his early efforts to obtain XAS spectra for AlC_x materials at the Advanced Light Source (beamline 7.3.1) which were unsuccessful. The XAS measurements reported herein were performed by Tom Regier at the Canadian Light Source, a national research facility of the University of Saskatchewan, which is supported by the Canada Foundation for Innovation (CFI), the Natural Sciences

and Engineering Research Council (NSERC), the National Research Council (NRC), the Canadian Institutes of Health Research (CIHR), the Government of Saskatchewan, and the University of Saskatchewan. We thank Sophia Randak for performing the Raman spectroscopy measurements. We also thank the Montana Nanotechnology Facility (MONT, an NNCI facility supported by National Science Foundation grant ECCS-1542210) for the use of their instrumentation. We gratefully acknowledge funding from the National Science Foundation Research Experiences for Undergraduates (REU) program (CHE-1852214), the Caltech Summer Undergraduate Research Fellowships (SURF) program, and research expansion funding (REF) provided by Montana State University.

Author contributions

All authors contributed equally to this work.

Funding

Financial support was provided by the National Science Foundation, the California Institute of Technology, and Montana State University.

Data availability

All supporting data are provided in the Supporting Information.

Declarations

Conflict of interest

None.

Supplementary Information

The online version contains supplementary material available at <https://doi.org/10.1557/s43579-024-00531-w>.

Open Access

This article is licensed under a Creative Commons Attribution 4.0 International License, which permits use, sharing, adaptation, distribution and reproduction in any medium or format, as long as you give appropriate credit to the original author(s) and the source, provide a link to the Creative Commons licence, and indicate if changes were made. The images or other third party material in this article are included in the article's Creative Commons licence, unless indicated otherwise in a credit line to the material. If material is not included in the article's Creative Commons licence and your intended use is not permitted by statutory regulation or exceeds the permitted use, you will need to obtain permission directly from the copyright holder. To view a copy of this licence, visit <http://creativecommons.org/licenses/by/4.0/>.

References

1. S. M. Sze, Y. Li, and K. K. Ng, *Physics of Semiconductor Devices*, 4 ed. Wiley, 2021, p. 944.
2. R. Leyva Ramos, J. Ovalle-Turrubiarres, M.A. Sanchez-Castillo, Adsorption of fluoride from aqueous solution on aluminum-impregnated carbon. *Carbon* **37**(4), 609–617 (1999). [https://doi.org/10.1016/S0008-6223\(98\)00231-0](https://doi.org/10.1016/S0008-6223(98)00231-0)
3. K. Landry, S. Kalogeropoulou, N. Eustathopoulos, Wettability of carbon by aluminum and aluminum alloys. *Mater. Sci. Eng. A* **254**(1), 99–111 (1998). [https://doi.org/10.1016/S0921-5093\(98\)00759-X](https://doi.org/10.1016/S0921-5093(98)00759-X)
4. T. Etter, P. Schulz, M. Weber, J. Metz, M. Wimpler, J.F. Löffler, P.J. Uggowitzer, Aluminium carbide formation in interpenetrating graphite/aluminium composites. *Mater. Sci. Eng. A* **448**(1), 1–6 (2007). <https://doi.org/10.1016/j.msea.2006.11.088>
5. M.H. Vidal-Sétif, M. Lancin, C. Marhic, R. Valle, J.L. Raviart, J.C. Daux, M. Rabinovitch, On the role of brittle interfacial phases on the mechanical properties of carbon fibre reinforced Al-based matrix composites. *Mater. Sci. Eng. A* **272**(2), 321–333 (1999). [https://doi.org/10.1016/S0921-5093\(99\)00487-6](https://doi.org/10.1016/S0921-5093(99)00487-6)
6. S. Ullah et al., Direct synthesis of large-area Al-doped graphene by chemical vapor deposition: advancing the substitutionally doped graphene family. *Nano Res.* **15**(2), 1310–1318 (2021). <https://doi.org/10.1007/s12274-021-3655-x>
7. M. Nairat, J.A. Talla, Electronic properties of aluminum doped carbon nanotubes with stone wales defects: density functional theory. *Solid State Phys.* **61**(10), 1896–1903 (2019). <https://doi.org/10.1134/S1063783419100421>
8. R. Wang, D. Zhang, W. Sun, Z. Han, C. Liu, A novel aluminum-doped carbon nanotubes sensor for carbon monoxide. *J. Mol. Struct.* **806**(1), 93–97 (2007). <https://doi.org/10.1016/j.theochem.2006.11.012>
9. Z.M. Ao, T.T. Tan, S. Li, Q. Jiang, Molecular hydrogen storage in Al-doped bulk graphite with wider layer distances. *Solid State Commun.* **149**(33), 1363–1367 (2009). <https://doi.org/10.1016/j.ssc.2009.05.022>
10. T. Jeon, S. Lee, S.C. Jung, Boron-, nitrogen-, aluminum-, and phosphorus-doped graphite electrodes for non-lithium ion batteries. *Curr. Appl. Phys.* **20**(8), 988–993 (2020). <https://doi.org/10.1016/j.cap.2020.06.017>
11. A. Shokuhi Rad, Y.M. Jouibary, V.P. Foukoliaei, E. Binaeian, Study on the structure and electronic property of adsorbed guanine on aluminum doped graphene: first principles calculations. *Curr. Appl. Phys.* **16**(5), 527–533 (2016). <https://doi.org/10.1016/j.cap.2016.02.004>
12. Z.M. Ao, J. Yang, S. Li, Q. Jiang, Enhancement of CO detection in Al doped grapheme. *Chem. Phys. Lett.* **461**(4), 276–279 (2008). <https://doi.org/10.1016/j.cplett.2008.07.039>
13. Z.M. Ao, Q. Jiang, R.Q. Zhang, T.T. Tan, S. Li, Al doped graphene: a promising material for hydrogen storage at room temperature. *J. Appl. Phys.* (2009). <https://doi.org/10.1063/13103327>
14. W. Zhao, Q.Y. Meng, Adsorption of methane on pristine and al-doped graphene: a comparative study via first-principles calculation. *Adv. Mat. Res.* **602–604**, 870–873 (2012). <https://doi.org/10.4028/www.scientific.net/AMR.602-604.870>
15. A. Shokuhi Rad, V. Pouralijan Foukoliaei, Density functional study of Al-doped graphene nanostructure towards adsorption of CO, CO₂ and H₂O. *Synth. Met.* **210**, 171–178 (2015). <https://doi.org/10.1016/j.synthmet.2015.09.026>
16. S.S. Varghese, S. Swaminathan, K.K. Singh, V. Mittal, Ab initio study on gas sensing properties of group III (B, Al and Ga) doped graphene. *Comput. Condens. Matter* **9**, 40–55 (2016). <https://doi.org/10.1016/j.cocom.2016.09.004>
17. Y.H. Tian, S. Hu, X. Sheng, Y. Duan, J. Jakowski, B.G. Sumpter, J. Huang, Non-transition-metal catalytic system for N(2) reduction to NH(3): a density functional theory study of Al-doped graphene. *J. Phys. Chem. Lett.* **9**(3), 570–576 (2018). <https://doi.org/10.1021/acs.jpclett.7b03094>
18. D. Shahabi, H. Tavakol, A DFT study on the catalytic ability of aluminum doped graphene for the initial steps of the conversion of methanol to gasoline. *Comput. Theor. Chem.* **1127**, 8–15 (2018). <https://doi.org/10.1016/j.comptc.2018.02.001>
19. N.A. Gokcen, L.L. Oden, Phase equilibria in aluminum-carbon system at high temperatures. *Ber. Bunsenges. Phys. Chem.* **102**(9), 1178–1180 (2010)

20. N.P. Stadie, E. Billeter, L. Piveteau, K.V. Kravchyk, M. Döbeli, M.V. Kovalenko, Direct synthesis of bulk boron-doped graphitic carbon. *Chem. Mater.* **29**(7), 3211–3218 (2017). <https://doi.org/10.1021/acs.chemmater.7b00376>
21. D. McGlamery, C. McDaniel, D. M. Ladd, M. A. Mosquera, M. T. Mock, and N. P. Stadie, Precursor Decomposition Compatability as the Key to the Halide-Free Synthesis of Metastable BC₃. (*submitted*), (2023)
22. E. Billeter, D. McGlamery, M. Aebli, L. Piveteau, M.V. Kovalenko, N.P. Stadie, Bulk phosphorus-doped graphitic carbon. *Chem. Mater.* **30**(14), 4580–4589 (2018)
23. H. Schneider, J. Schreuer, B. Hildmann, Structure and properties of mullite—a review. *J. Eur. Ceram. Soc.* **28**(2), 329–344 (2008). <https://doi.org/10.1016/j.jeurceramsoc.2007.03.017>
24. D. McGlamery, A.A. Baker, Y.-S. Liu, M.A. Mosquera, N.P. Stadie, Phonon dispersion relation of bulk boron-doped graphitic carbon. *J. Phys. Chem. C* **124**(42), 23027–23037 (2020)
25. L. Andrini, M.R. Gauna, M.S. Conconi, G. Suarez, F.G. Requejo, E.F. Aglietti, N.M. Rendtorff, Extended and local structural description of a kaolinitic clay, its fired ceramics and intermediates: an XRD and XANES analysis. *Appl. Clay Sci.* **124–125**, 39–45 (2016). <https://doi.org/10.1016/j.clay.2016.01.049>
26. G. Küper et al., Aluminum K-edge absorption (XANES) studies of noncrystalline mullite precursors. *J. Am. Ceram. Soc.* **79**(3), 813–816 (2005). <https://doi.org/10.1111/j.1151-2916.1996.tb07952.x>
27. A. Omega, R. Prins, J.A. van Bokhoven, Effect of temperature on aluminum coordination in zeolites H–Y and H–USY and amorphous Silica–Alumina: An in situ Al K edge XANES study. *J. Phys. Chem. B* **109**(19), 9280–9283 (2005). <https://doi.org/10.1021/jp050086o>
28. A.B. Altman et al., Chemical and morphological inhomogeneity of aluminum metal and oxides from soft X-ray spectromicroscopy. *Inorg. Chem.* **56**(10), 5710–5719 (2017). <https://doi.org/10.1021/acs.inorgchem.7b00280>
29. D.W. Squire, Mechanistic studies of the decomposition of trimethylaluminum on heated surfaces. *J. Vac. Sci. Technol.* (1985). <https://doi.org/10.1116/1.582976>
30. Z. Zhang, Y. Pan, J. Yang, Z. Jiang, H. Fang, Experimental study of trimethyl aluminum decomposition. *J. Cryst. Growth* **473**, 6–10 (2017). <https://doi.org/10.1016/j.jcrysgro.2017.05.020>

Publisher's Note Springer Nature remains neutral with regard to jurisdictional claims in published maps and institutional affiliations.